Photoinduced Phase Transitions by Time-Resolved Far-Infrared Spectroscopy in V_{2}O_{3}

M. K. Liu, B. Pardo, J. Zhang, M. M. Qazilbash, Sun Jin Yun, Z. Fei, Jun-Hwan Shin, Hyun-Tak Kim, D. N. Basov, and R. D. Averitt

Phys. Rev. Lett. **107**, 066403 — Published 3 August 2011

DOI: 10.1103/PhysRevLett.107.066403

Photoinduced phase transitions by time-resolved far-infrared spectroscopy in V_2O_3

M. K. Liu,[1] B. Pardo,[1] J. Zhang,[1] M. M. Qazilbash,[2] Sun Jin Yun,[3,4] Y. Fei,[2] Junhwan Shin,[4] Hyun-Tak Kim,[3,4] D. N. Basov,[2] and R. D. Averitt[1,*]

[1]*Boston University, Department of Physics, 590 Commonwealth Ave, Boston, Massachusetts, 02215*
[2]*Department of Physics, University of California, San Diego, La Jolla, California 92093*
[3]*Metal-Insulator Transition Lab, ETRI, Daejeon 305-350, South Korea*
[4]*School of Advanced Device Technology, University of Science and Technology, Daejeon 305-333, South Korea*

(Dated: June 29, 2011; Received)

Using time resolved far-infrared spectroscopy, we observe multiple routes for photoinduced phase transitions in V_2O_3. This includes (i) a photothermal antiferromagnetic to paramagnetic transition and (ii) an incipient strain generated paramagnetic metal to paramagnetic insulator transition which manifests as coherent oscillations in the far-infrared conductivity. The ∼100 ps conductivity oscillation results from coherent acoustic phonon modulation of the bandwidth W. Our results indicate that poor metals are particularly amenable to coherent strain control of their electronic properties.

V_2O_3, a canonical Mott-Hubbard system, is an example of a correlated electron material with an intriguing phase diagram studied thoroughly during last few decades [1–3]. It includes two high temperature phases - paramagnetic insulator and paramagnetic metal - and a low temperature antiferromagnetic insulating phase. Time-integrated optical conductivity measurements have played an important role in elucidating the electronic properties. There is a strong temperature dependence of the spectral weight and a Drude-like quasiparticle peak in the metallic phase disappears in the low (<150K) and high (doped/stressed) temperature insulating phase. The spectral weight is not recovered up to 6eV revealing its strongly correlated nature [4, 5].

Recent studies highlight that while Mott-Hubbard physics provides the backdrop for understanding the metal-insulator transition, subtleties abound [6–11]. Multi-orbital interactions are crucial for a complete understanding and are sensitively influenced by slight static or dynamic changes in the lattice with the consequence that multiple pathways for a phase transition are possible [12]. Time-resolved optical spectroscopy provides a powerful approach to interrogate potential pathways for phase transitions [13–17].

We present time-resolved far-infrared conductivity studies on V_2O_3 probing phase transition dynamics following photoexcitation. We observe a ∼20 ps photoinduced antiferromagnetic insulator (AI) to paramagnetic metal (PM) transition. In addition, in the metallic phase a strain generated incipient PM to paramagnetic insulator (PI) transition manifests as coherent oscillations in the far-infrared conductivity. The ∼100 ps conductivity oscillation results from coherent acoustic phonon modulation of the bandwidth W. In the metallic state of V_2O_3 W is comparable to the on-site Coulomb repulsion U. The observation of this response in V_2O_3 indicates that poor metals with large U/W ($\gtrsim$1) are amenable to coherent strain control of their electronic properties. From a microscopic perspective, dynamical spectral weight transfer results from coherent strain modification of the orbital interactions of the trigonal split vanadium t_{2g} levels.

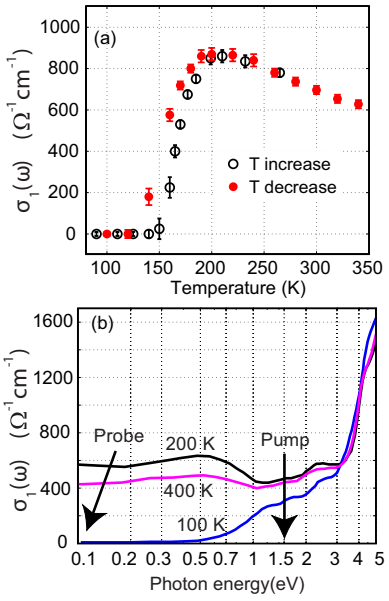

FIG. 1: (a) Temperature dependence of far-infrared conductivity of V_2O_3 thin film measured by THz-TDS. (b) Real part of the optical conductivity as a function of photon energy for various temperatures. The arrows indicate the spectral range for the pump and probe pulses for the far-infrared time-resolved experiments.

Our V_2O_3 samples are 75 nm thick and are grown on oriented sapphire substrates [18]. The films were confirmed by x-ray diffraction to be single phase V_2O_3 and have been characterized using optical conductivity measurements [4]. Optical-pump THz-probe measurements were performed with a regenerative amplifier producing 35 fs 3.5 mJ pulses centered at 1.55 eV (800 nm). The THz pulses were generated and detected using electro-optic techniques [16]. All-optical pump-probe measurements were performed using the same experiment to enable direct comparison of photoinduced changes in the

real part of the far-infrared conductivity ($\Delta\sigma_1$) and reflectivity (ΔR/R) at 1.55 eV.

Initial measurements using THz-TDS (i.e. without photoexcitation) were performed to measure the far-infrared conductivity (σ_1, coherent Drude response) as a function of temperature. Figure 1(a) shows the film transitions from the AI phase to the PM phase at approximately T_{MIT}=150K. Below T_{MIT}, the far-infrared response vanishes as spectral weight shifts to higher frequencies (see also 100K data in Fig. 1(b)). In the correlated metallic phase above T_{MIT}, a maximum conductivity of 850$(\Omega\text{cm})^{-1}$ is obtained at 200K. From 200K to 400K, the conductivity decreases with temperature, consistent with previous work [1, 4, 7].

Figure 1(b) shows the optical conductivity from the far-infrared to 6 eV at 100, 200, and 400 K [4]. Between 400K and 200K there is an increase in the spectral weight below 1 eV. Below T_{MIT} a gap is clearly observed. Trigonal distortion of the tetrahedrally coordinated vanadium ions lifts the degeneracy of the t_{2g} orbitals leading to non-degenerate a_{1g} and double degenerate e_g^π bands. The spectral features in the 0 - 3 eV range arise from transitions in these bands augmented by strong on-site Coulomb repulsion [4, 7]. Thus, the pump and probe pulses primarily excite and interrogate the vanadium d-orbital manifold.

Figure 2 displays the results of optical-pump terahertz-probe (OPTP) measurements. The incident pump fluence is 1 mJ/cm^2, corresponding to an absorbed energy density of ~100 J/cm^3. This yields an excitation density of approximately 0.1 electron per unit cell. The initially excited electron distribution relaxes on a picosecond timescale through electron-phonon thermalization leading to an increase in the temperature of the sample on this timescale. Figure 2(a) shows the temporal evolution of σ_1 (plotted as the change in conductivity, $\Delta\sigma_1(\tau)$) at various initial temperatures (T_i) following photoexcitation. As Fig. 2(a) shows, at T_i=140K σ_1 increases with time as the sample evolves toward the metallic state. The conductivity reaches a plateau after ~ 100ps. On a longer timescale (not shown) heat is transferred to the substrate and σ_1 recovers to its initial value. For T_i > 140K, there is a decrease in the magnitude of $\Delta\sigma_1$, reaching a minimum at ~185K and crossing over to a photoinduced decrease in the conductivity. Pronounced ~100ps conductivity oscillations manifest in the metallic state and will be discussed in detail below.

Prior to discussing the origin of the metallic phase conductivity modulation, we consider the transition dynamics from AI to PM. In Fig. 2(a), the magnitude of $\Delta\sigma_1$ decreases with increasing T_i consistent with the notion of heating with $\Delta\sigma \propto 1 - \sigma(T_f)/\sigma(200\text{K})$ where $T_f = T_i + \Delta T$ is the final temperature. ΔT is the induced temperature change which goes as $\Delta T = \xi/C(T)$ where ξ is the absorbed energy density and C(T) is the specific heat. However, V_2O_3 has a first order structural phase

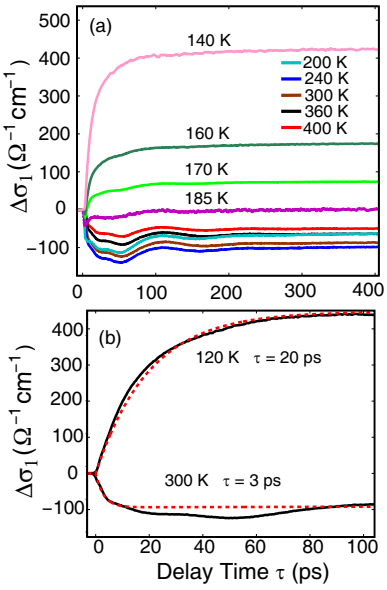

FIG. 2: (a)THz conductivity dynamics as a function of delay time (τ) at various temperatures.(b) Risetime dynamics at 120K and 300K. The black lines are experimental data and the red dashed lines fits to a single exponential.

transition with an associated latent heat (70J/cm^3[19]) yielding a sharp decrease in ΔT near T_{MIT} (see supplementary material for further details). For an absorbed energy density of 100 J/cm^3, 70% is needed to overcome the latent heat. This is why at 185K there is virtually no change in the conductivity except for the (nonthermal) oscillatory response. The latent heat plays an important role in determining the fluence threshold and has also been observed in VO_2.

A bottleneck in the dynamics associated with the latent heat also manifests in the risetime of the conductivity following photoexcitation as shown in Fig. 2(b). In the AI phase, the risetime is ~20ps which is considerably longer than the time for electron-phonon thermalization. This behavior has been observed in VO_2 consistent with nucleation and percolative growth of the metallic phase upon rapid heating into the metallic state [16]. The need for an energy density in excess of the latent heat and percolative kinetics determine the timescale for the final state electronic properties to manifest in a photothermal transition. In the metallic state, this risetime decreases to 3ps (~1ps resolution limited) due to electron phonon relaxation. This is faster than the 20ps risetime observed when starting from the insulating state and highlights the absence of percolative dynamics in the metallic phase.

In addition to thermal effects initiated on a picosecond timescale due to electron-phonon thermalization, there are nonthermal effects. The pronounced oscillations of $\Delta\sigma_1$ that arises in the metallic phase represents such a response. The oscillation period is consistent with a co-

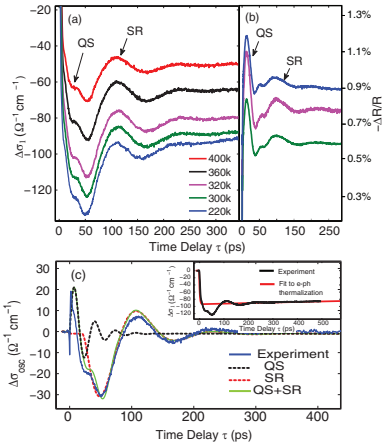

FIG. 3: (a) $\Delta\sigma_1$ as a function of pump-probe delay. QS labels the quasi-shear wave, and SR the surface Rayleigh wave. (b) ΔR/R with 1.55 eV probe showing a one to one correspondence with $\Delta\sigma$. (c) Fit to the $\Delta\sigma_{osc}$ at 300K using the known frequencies of the QS and SR [27]. The inset is a fit to the initial risetime dynamics which is subtracted from the oscillatory component.

herent acoustic phonons, but as far-infrared modulation of σ_1 has not previously been observed, it is important to investigate its origin. To accomplish this, we performed all optical pump-probe measurements where the theory and interpretation of coherent acoustic oscillations is well developed [20, 21].

In Figure 3(a) we show an expanded view of $\Delta\sigma_1$ in the metallic state of V_2O_3. Pronounced conductivity oscillations at all temperatures in the PM phase are observed. Figure 3(b) shows the results of degenerate optical-pump optical-probe measurements of the photoinduced reflectivity change (ΔR/R) at 1.55eV. The fluence of the pump beam and probe beams are $1\text{mJ}/cm^2$ and $10\mu\text{J}/cm^2$, respectively. The oscillations in ΔR/R show a one to one correspondence to the conductivity oscillations.

A detailed understanding of coherent acoustic phonon induced modulation of ΔR/R has been developed [20–25]. Inhomogeneous excitation due to the finite penetration depth of the pump pulse generates, following rapid electron-phonon thermalization, a non-uniform lattice displacement normal to the sample surface. This lattice displacement induces a longitudinal strain wave resulting in a dielectric discontinuity that propagates at the sound velocity. The resultant ΔR/R modulation arises from the probe pulse reflected off the surface interfering with the reflection off of the propagating dielectric discontinuity. The change in reflectivity ΔR is described by the expression:

$$\Delta R(t) = \int_0^{z_0} f(z)\eta(z,t)dz \qquad (1)$$

where η is the strain introduced by the lattice displacement, z_0 is the thickness of the film and $f(z)$ is the sensitivity function introduced by Thomsen et al [21]. The sensitivity function is fairly complex and includes derivatives of the refractive index with respect to η.

For the induced modulation in σ_1, the situation is different in that an interference effect cannot be the origin of the oscillatory signal. The far-infrared probe wavelength ($1\text{THz} \rightarrow 300\mu\text{m}$) is orders of magnitude greater than the film thickness. Further, with transmission measurements we directly measure σ_1. Thus, the oscillatory part in Fig. 3(a) is described by the following equation:

$$\Delta\sigma_{osc}(t) = \int_0^{z_0} \frac{\partial\sigma_1}{\partial\eta}\eta(z,t)dz \qquad (2)$$

where $\partial\sigma_1/\partial\eta$ is the derivative of the conductivity with respect to strain which is of microscopic origin.

For 75nm thin films, the strain waves are not well separated in time. Nonetheless, we are able to identify the oscillatory modes that modulate the conductivity. There are two components labeled as quasi-shear (QS) and surface Rayleigh (SR) in Figure 3. This assignment derives from fits to the data using the frequencies of the acoustic modes in V_2O_3 as determined from Brillouin scattering studies [27].

In Figure 3(c) we plot $\Delta\sigma_{osc}(t)$ as the oscillatory conductivity change by subtracting the thermal component from experimental data at 300K. The subtraction is shown in the inset where the red line is a fit with the two temperature model to determine the thermally induced change of σ_1. $\Delta\sigma_{osc}(t)$ (blue) is fitted to two components consisting of a dominant SR mode with a period of 130ps (8GHz) and a QS mode with a period of 30ps (33GHz) consistent with Ref. [27]. The sum of these two components (green) provides an excellent fit to the data. The contributions of each] are comparable though of opposite phase.

The resulting SR and QS mode response results from mode conversion of an initially excited longitudinal strain which likely occurs at the sample-substrate interface. These strain waves correspond to a lattice displacement on the order of 10^{-13} m, and an induced stress (for a 1 mJ/cm^2 excitation fluence) on the order of 0.5 kbar [10, 19, 27, 28]. This stress yields a $\Delta\sigma_1/\sigma_1$ of approximately 4% and ΔR/R at 1.55 eV of -0.2%.

The conductivity oscillation is consistent with strain induced modulation of the spectral weight where a decrease (increase) in σ_1 corresponds to driving the V_2O_3 towards (away from) the paramagnetic insulating state. In the PM phase, V_2O_3 is particularly sensitive to small perturbations since the on-site Coulomb repulsion U is comparable to the electronic bandwidth W, which has a exponential dependence on the atomic displacement.

Figure 4(a) maps the photothermal AI/PM transition (red arrow) and strain-induced PM/PI transition (blue arrow) onto the phase diagram of V_2O_3 highlighting that

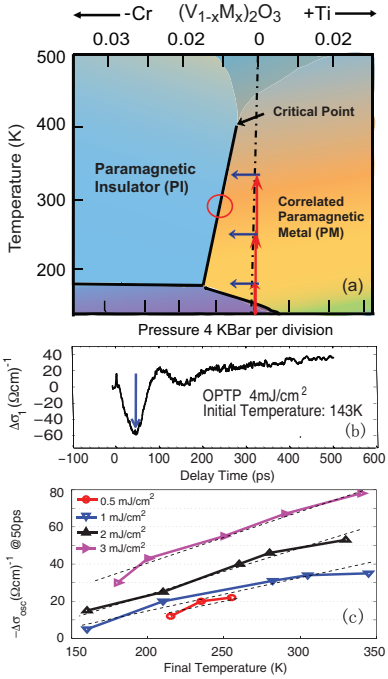

FIG. 4: (a) Summary of the dynamics indicated on the phase diagram of V_2O_3. Red arrows indicate rapid electron phonon relaxation drives V_2O_3 into the metallic state; blue arrows illustrate the subsequent oscillations correspond to dynamically tuning the strain environment. (b) One example of OPTP at initial temperature of 143K which a pump fluence 4mJ/cm2, the blue arrow indicates the conductivity deduction induced by the strain wave only. (c) Peak conductivity reduction ($\Delta\sigma_{osc}(t)$ at 50ps) versus pump fluence and final temperature.

two unique pathways are possible. The AI→PM→PI transition precursor is clearly shown in Fig. 4(b). At an optimally chosen initial temperature (143 K, semiconducting region) and pump fluence (4 mJ/cm^2), the peak conductivity reduction at 50ps delay time is purely induced by a tensile strain followed by laser excitation. In Fig.4(c) we perform a detailed study of this peak conductivity reduction ($\Delta\sigma_{osc}(t)$ at 50ps) versus pump fluence and final temperature. This yields three pieces of useful information: i) for the same pump fluence, the higher the final temperature the larger the conductivity decrease. This is in accordance with the slope of the PM/PI phase boundary (Fig. 4 (a)). The higher the final temperature, the closer the subsequent strain dynamics would bring the system towards insulating state. ii) At the same final temperature, a larger fluence assures a larger conductivity decreases as this generates a larger amplitude strain wave. iii) In order to achieve a sufficient strain (∼4kbar) to fully drive the PM/PI phase transition would require more than 10 mJ/cm^2 pump fluence causing irreversible damage to the film (damage threshold is ∼8 mJ/cm^2). Thus, it would be of interest to interrogate the phase transition dynamics in doped samples closer to the transition boundary as indicated in the Fig. 4 (red circle).

In summary, photoinduced temperature changes and photoinduced strain provide unique pathways in driving phase transitions in V_2O_3. Further, these mechanisms may provide a powerful approach to tune correlated electron materials to novel metastable phases with order parameters that are not thermally accessible providing a complementary approach to photodoping [29–31].

Acknowledgement: We would like to acknowledge support from DOE-BES for this work under grant DE-FG02-09ER46643, DE-FG02-00ER45799, and ETRI.

* Electronic address: raveritt@physics.bu.edu

[1] D. B. McWhan, et al., Phys. Rev. Lett., **23**, 24 (1969).
[2] D. B. McWhan, et al., Phys. Rev. Lett.**27**, 14 941 (1971).
[3] P. Limelette, et al., Science **302**, 89 (2003).
[4] M. M. Qazilbash, et al., Phys. Rev. B **77**, 115121 (2008).
[5] L. Baldassarre, et al., Phys. Rev. B **77**, 113107 (2008).
[6] M.Imada, A. Fujimori and Y.Tokura, Rev. Mod. Phys. **70**,1039 (1998).
[7] G. Kotliar, et al., Rev. Mod. Phys. **78**, 865 (2006).
[8] A. Tanaka, J. Phys. Soc. Jpn. **71**, 1091 (2002).
[9] M. S. Laad, et al.,, Phys. Rev. B **73**,045109 (2006).
[10] P.Pfalzer, et al., Phys. Rev. B **73**, 144106 (2006).
[11] P. Fazekas, Lecture Notes on Electron Correlation and Magnetism, World Scientific (1999).
[12] F. Rodolakis, et al., Phys. Rev. Lett. **104**, 047401 (2010).
[13] A. Cavalleri, et al., Phys. Rev. Lett. **95**, 067405 (2005).
[14] D. J. Hilton, et al., Phys. Rev. Lett. **99**, 226401 (2007).
[15] K. C. Kubler, et al., Phys. Rev. Lett. **99**, 116401 (2007).
[16] R.D. Averitt, A. J. Taylor, J. Phys: Condens. Matt. **14**, R1357 (2002).
[17] D. N. Basov, et al., Rev. Mod. Phys. **83**, 471 (2011).
[18] S. J. Yun, et al., J. Jpn. Appl. Phys. **48**, 04C139 (2009).
[19] H.V.Keer, et al., J. Sol. St. Chem. **19**, 95-102 (1976).
[20] C. Thomsen, et al., Phys. Rev. Lett. **53**, 989 (1984).
[21] C. Thomsen, et al. Phys. Rev. B **34**, 4129 (1986).
[22] O.B.Wright, Phys. Rev. B **49** 14 (1994).
[23] O. Matsuda, et al., Phys. Rev. Lett. **93**, 095501 (2004).
[24] D. Lim, et al., Phys. Rev. B **71**, 134403 (2005).
[25] T. Pezeril, et al., Phys. Rev. B **75**, 174307 (2007).
[26] G. Keller, et al., Phys Rev B **70**, 205116 (2004).
[27] Md. Motin Seikh, et al, Solid State Comm. **138**, 466 (2006).
[28] B. S. Allimi, et al., Appl. Phys. Lett. **93**, 112109 (2008).
[29] K. Nasu, Photoinduced Phase Transitions. Singapore: World Scientific, 2004.
[30] P. Baum, D.-S. Yang, A. H. Zewail, Science **318**, 788 (2007).
[31] Hyun-Tak Kim, et al., Phys. Rev. Lett **97**, 266401 (2006).